



Area-preserving maps models of gyroaveraged $E \times B$ chaotic transport

J. D. da Fonseca, D. del-Castillo-Negrete, and I. L. Caldas

Citation: *Physics of Plasmas* (1994-present) **21**, 092310 (2014); doi: 10.1063/1.4896344

View online: <http://dx.doi.org/10.1063/1.4896344>

View Table of Contents: <http://scitation.aip.org/content/aip/journal/pop/21/9?ver=pdfcov>

Published by the [AIP Publishing](#)

Articles you may be interested in

[Gyroaverage effects on chaotic transport by drift waves in zonal flows](#)

Phys. Plasmas **20**, 022303 (2013); 10.1063/1.4790639

[Dynamics and transport in mean-field coupled, many degrees-of-freedom, area-preserving nontwist maps](#)

Chaos **22**, 013137 (2012); 10.1063/1.3694129

[Transport properties in nontwist area-preserving maps](#)

Chaos **19**, 043108 (2009); 10.1063/1.3247349

[Finite Larmor radius effects on nondiffusive tracer transport in a zonal flow](#)

Phys. Plasmas **15**, 102309 (2008); 10.1063/1.3003072

[Hypersonic drift-tearing magnetic islands in tokamak plasmas](#)

Phys. Plasmas **14**, 122502 (2007); 10.1063/1.2811928

The advertisement for the COMSOL Conference 2014 Boston is set against a blue background. On the left, the text 'COMSOL CONFERENCE 2014 BOSTON' is displayed in white. The central text reads 'The Multiphysics Simulation Event of the Year' in a large, white, sans-serif font. To the right, there is a graphic of a toroidal magnetic field with two central plasma columns, rendered in blue and yellow. A white button with the text 'LEARN MORE >>' is positioned over the top right of the graphic. The COMSOL logo is located in the bottom right corner of the advertisement.

Area-preserving maps models of gyroaveraged $\mathbf{E} \times \mathbf{B}$ chaotic transport

J. D. da Fonseca,^{1,a)} D. del-Castillo-Negrete,^{2,b)} and I. L. Caldas^{1,c)}

¹*Institute of Physics, University of São Paulo, São Paulo, SP 5315-970, Brazil*

²*Oak Ridge National Laboratory, Oak Ridge, Tennessee 37831-8071, USA*

(Received 15 July 2014; accepted 9 September 2014; published online 29 September 2014)

Discrete maps have been extensively used to model 2-dimensional chaotic transport in plasmas and fluids. Here we focus on area-preserving maps describing finite Larmor radius (FLR) effects on $\mathbf{E} \times \mathbf{B}$ chaotic transport in magnetized plasmas with zonal flows perturbed by electrostatic drift waves. FLR effects are included by gyro-averaging the Hamiltonians of the maps which, depending on the zonal flow profile, can have monotonic or non-monotonic frequencies. In the limit of zero Larmor radius, the monotonic frequency map reduces to the standard Chirikov-Taylor map, and in the case of non-monotonic frequency, the map reduces to the standard nontwist map. We show that in both cases FLR leads to chaos suppression, changes in the stability of fixed points, and robustness of transport barriers. FLR effects are also responsible for changes in the phase space topology and zonal flow bifurcations. Dynamical systems methods based on the counting of recurrences times are used to quantify the dependence on the Larmor radius of the threshold for the destruction of transport barriers. © 2014 AIP Publishing LLC. [<http://dx.doi.org/10.1063/1.4896344>]

I. INTRODUCTION

Important research efforts in controlled nuclear fusion are focused on the magnetic confinement of hot plasmas. In order to improve the confinement conditions, a better understanding of the particle transport is needed, especially in the case of particle drift motion. A standard approach to this problem is based on the $\vec{E} \times \vec{B}$ approximation of charged particle's guiding center's motion, e.g., Refs. 1–4. However, in the case of fast particles, e.g., alpha particles in burning plasmas or in the presence of inhomogeneous fields on the scale of the Larmor radius, it is necessary to consider finite Larmor radius (FLR) effects to correctly estimate the transport of particles.^{5,6}

Previous studies on the role of the Larmor radius on transport include Refs. 5, 7, and 8 where particle transport in numerical simulations of electrostatic turbulence was analyzed and FLR effects were shown to inhibit transport. The problem of non-diffusive chaotic transport and fractional diffusion in the presence of FLR effects was addressed in Ref. 9. In Refs. 6 and 10, dynamical systems methods were used to investigate FLR effects on chaos suppression and bifurcations in the phase space topology.

In this paper, we study FLR effects in the context of simplified area-preserving maps models of $\vec{E} \times \vec{B}$ motion. The maps are constructed following the standard Hamiltonian framework for electrostatic drift motion,¹¹ and FLR corrections are included by gyro-averaging the electrostatic potential.¹² The potential has an equilibrium depending on the radial coordinate and a time-dependent perturbation consisting of a linear superposition of drift waves. Depending on the radial dependence of the equilibrium

potential, the maps' frequencies can have monotonic or non-monotonic profiles. Our main focus is the study of FLR effects on chaos suppression, stability of fixed points, nontwist phase space topologies, and transport barriers. Although $\nabla \vec{B} \times \vec{B}$ drift might play a role in the presence of FLR, here, we will restrict attention to $\vec{E} \times \vec{B}$ drifts.

In dynamical systems theory, the term “nontwist” is used to designate Hamiltonian systems that violate the twist or non-degeneracy condition. A paradigmatic example is a perturbed system, in which the frequency of the unperturbed part of the Hamiltonian is a non-monotonic function of the action. Nontwist Hamiltonian systems are found in many physical systems including $\mathbf{E} \times \mathbf{B}$ transport in magnetized plasmas,^{3,4} magnetic fields with reverse shear in toroidal plasma devices,^{13–16} and transport by traveling waves in shear flows^{17–19} among others. The presence of nontwist transport barriers (NTBs) is among the most important properties of nontwist Hamiltonian systems. By nontwist transport barriers, we mean a robust region of invariant circles, also called Kolmogorov-Arnold-Moser (KAM) curves, which are very resilient to breakup, i.e., they can survive even when the phase space is almost completely chaotic. This property, originally discovered in Refs. 17 and 20, has also been referred to as strong KAM stability²¹ in the context of one-and-a-half degrees-of-freedom Hamiltonian systems, and has been the subject of several studies (see, for example, Refs. 22–25, and references therein). Throughout this paper we use the term “KAM curve” as a synonymous of “invariant circle” or “transport barrier.”

In this paper, the maps correspond to Hamiltonians whose unperturbed frequencies can be monotonic or non-monotonic functions of the action variable. The latter case is characterized by the presence of nontwist transport barriers that can be destroyed or restored by changing the value of the Larmor radius. This property is directly related to the FLR suppression of chaotic transport studied in Refs. 6 and 10. Here, we show

^{a)}Electronic mail: jfonseca@if.usp.br

^{b)}Electronic mail: delcastillod@ornl.gov

^{c)}Electronic mail: ibere@if.usp.br

that chaos suppression occurs when the Larmor radius is close to specific values, for which invariant circles become very resilient to breakup. In the case of nontwist maps, the invariant circles forming the nontwist transport barrier are the easiest to restore and the hardest to break. One of the main goals of the present work is the numerical computation of the critical parameters for the breakup of nontwist barriers. To compute the breakup diagrams, we follow the technique in Ref. 26, which is based on the application of Slater's theorem³⁸ to the recurrence properties of orbits. As shown in Refs. 26 and 27, the recurrence properties of an orbit provide an efficient and accurate method to differentiate chaotic and non-chaotic motion. A recent example of the application of this technique to the standard nontwist map was presented in Ref. 28.

The rest of the paper is organized as follows. Section II introduces a general area preserving map of gyro-averaged $\vec{E} \times \vec{B}$ transport. This model is the starting point for the specific cases studied in the subsequent sections. The first case, for which the frequency has a monotonic profile, is presented in Sec. III, where FLR effects on the transition to global chaos are analyzed. Section IV describes a case with a non-monotonic profile and discusses FLR effects on the stability of fixed points, phase space topology, and breakup diagrams. A second nontwist map is presented in Sec. V where FLR effects on zonal flow bifurcations are analyzed. Section VI presents the conclusions and a brief summary of the main results.

II. TRANSPORT MODEL

The $\vec{E} \times \vec{B}$ drift velocity of the guiding center is given by²⁹

$$\vec{v}_{GC} = \frac{\vec{E} \times \vec{B}}{B^2}. \quad (1)$$

Using x as radial coordinate, and y as poloidal coordinate, the equations of the $\vec{E} \times \vec{B}$ drift motion, $(\dot{x}(t), \dot{y}(t)) = \vec{v}_{GC}$, can be written as the Hamiltonian system

$$\frac{dx}{dt} = -\frac{\partial H(x, y, t)}{\partial y}, \quad \frac{dy}{dt} = \frac{\partial H(x, y, t)}{\partial x}, \quad (2)$$

where

$$H(x, y, t) = \frac{\phi(x, y, t)}{B_0}, \quad (3)$$

ϕ is the electrostatic potential and B_0 denotes the magnitude of the toroidal magnetic field, $\vec{B} = B_0 \hat{e}_z$. As discussed in Ref. 10, FLR effects can be incorporated substituting the electrostatic potential by its average over a circle around the guide center

$$\langle \phi(x, y, t) \rangle_\phi = \frac{1}{2\pi} \int_0^{2\pi} \phi(x + \rho \cos \varphi, y + \rho \sin \varphi, t) d\varphi, \quad (4)$$

where ρ is the Larmor radius. Equation (4) corresponds to the well-known gyro-averaging operation.¹² The gyro-averaged Hamiltonian can then be defined as

$$\langle H(x, y, t) \rangle_\phi = \frac{\langle \phi(x, y, t) \rangle_\phi}{B_0} \quad (5)$$

and the gyro-averaged equations of motion (2) can be written as

$$\frac{dy}{dt} = \frac{\partial \langle H \rangle_\phi}{\partial x}, \quad \frac{dx}{dt} = -\frac{\partial \langle H \rangle_\phi}{\partial y}. \quad (6)$$

Following Ref. 30, we assume an electrostatic potential of the form

$$\phi(x, y, t) = \phi_0(x) + A \sum_{m=-\infty}^{+\infty} \cos(ky - m\omega_0 t), \quad (7)$$

where $\phi_0(x)$ is the equilibrium potential, A , the amplitude of the drift waves, k is the wave number, and ω_0 is the fundamental frequency. Applying the gyro-average operation to Eqs. (4)–(7) and substituting the result in Eq. (3), we obtain the Hamiltonian

$$\langle H(x, y, t) \rangle_\phi = \langle H_0(x) \rangle_\phi + \frac{A}{B_0} J_0(k\rho) \sum_{m=-\infty}^{+\infty} \cos(ky - m\omega_0 t), \quad (8)$$

where J_0 is the zero-order Bessel function, and the integrable Hamiltonian $\langle H_0(x) \rangle_\phi$ is defined as

$$\langle H_0(x) \rangle_\phi = \frac{\langle \phi_0(x) \rangle_\phi}{B_0}. \quad (9)$$

Using the Fourier series representation of the Dirac delta function, Eq. (8) can be rewritten as

$$\begin{aligned} \langle H(x, y, t) \rangle_\phi &= \langle H_0(x) \rangle_\phi \\ &+ \frac{2\pi A}{B_0} J_0(k\rho) \cos(ky) \sum_{m=-\infty}^{+\infty} \delta(\omega_0 t - 2\pi m). \end{aligned} \quad (10)$$

Let $x_n = x(t_n^-)$ and $y_n = y(t_n^-)$, with $t_n^- = \frac{2\pi n}{\omega_0} - \varepsilon$, $n \in \mathbb{N}$ and $\varepsilon \rightarrow 0^+$. Integrating Eq. (6) in the interval (t_n^-, t_{n+1}^-) leads to the gyro-averaged drift wave map

$$x_{n+1} = x_n + \frac{2\pi k A}{\omega_0 B_0} J_0(\hat{\rho}) \sin(ky_n), \quad (11)$$

$$y_{n+1} = y_n + \frac{2\pi}{\omega_0} \Omega(x_{n+1}), \quad (12)$$

where $\hat{\rho} = k\rho$ and $\Omega(x)$ corresponds to the frequency associated to the integrable Hamiltonian in Eq. (9)

$$\Omega(x) = \frac{d\langle H_0(x) \rangle_\phi}{dx}. \quad (13)$$

For $\rho = 0$, $\Omega(x) = -E_r(x)/B_0$, where $E_r(x)$ is the radial component of the electric field. Depending on the equilibrium potential $\phi_0(x)$, which determines $E_r(x)$ and $\Omega(x)$, different area-preserving maps can be constructed from Eqs. (11) and (12). In Secs. III, IV and V, we discuss three different cases.

III. GYRO-AVERAGED STANDARD MAP (GSM)

As a first simple example, we assume a monotonic linear frequency profile to construct the GSM. This map is a modified version of the standard map, also known as the Chirikov-Taylor map^{31,32} To define the frequency in Eq. (12), we use the equilibrium potential

$$\phi_0(x) = \alpha \frac{(kx)^2}{2}, \tag{14}$$

where k is the wave number in Eq. (7) and α is a free parameter. Applying the gyro-average operation to Eq. (14) yields

$$\langle H_0(x) \rangle_\varphi = \frac{\alpha}{B_0} \left[\frac{(kx)^2}{2} + \frac{\hat{\rho}^2}{4} \right]. \tag{15}$$

Substituting Eq. (15) in Eq. (13), we get the frequency

$$\Omega(x) = \frac{\alpha k^2}{B_0} x, \tag{16}$$

which does not depend on the Larmor radius, and has a monotonic profile. Introducing the non-dimensional variables

$$I = k\gamma x, \quad \theta = ky, \tag{17}$$

and the constant

$$\gamma = \frac{2\pi\alpha k^2}{\omega_0 B_0}, \tag{18}$$

we get, from Eqs. (11) and (12), the GSM

$$I_{n+1} = I_n + K_{ef}(\hat{\rho}) \sin \theta_n, \tag{19}$$

$$\theta_{n+1} = \theta_n + I_{n+1}, \quad \text{mod } 2\pi, \tag{20}$$

where

$$K_{ef} = KJ_0(\hat{\rho}) \tag{21}$$

is the effective perturbation parameter and $K = \gamma^2 A/\alpha$ is the perturbation parameter. For $\hat{\rho} = 0$, $K_{ef} = K$, and the GSM reduces to the standard map.

The phase space of the GSM, as in the case of any area-preserving map, consists of periodic, quasiperiodic, and chaotic orbits. Quasiperiodic orbits cover densely invariant curves. The invariant curves around the elliptic fixed points form island chains, and the invariant curves that wind around the entire domain of the angle variable form invariant circles.³³ The presence of KAM curves is of special interest because they preclude transport in the direction of the radial coordinate x , keeping chaotic orbits confined to specific regions of phase space.

According to Green’s residue method,³⁴ the transition to global chaos in the standard map occurs when the absolute value of the perturbation parameter is equal to, or greater than, the critical value $K_c \simeq 0.9716$. That is, for $K \geq K_c$, all KAM curves are broken, and chaotic orbits can spread over all phase space (except in regions occupied by isolated

islands). Larmor radius effects on the transition to global chaos in the GSM can be analyzed by defining the critical line dividing the $K - \hat{\rho}$ parameter space in two regions: one for which the phase space contains at least one KAM curve and another for which transition to global chaos has occurred. In the standard map, there is no dependence on $\hat{\rho}$, which means that the critical line is just a horizontal line defined at $K = K_c$, as indicated in Fig. 1. However, for the GSM, the critical line is determined by the condition $|K_{ef}| = K_c$ which implies

$$K = \frac{K_c}{|J_0(\hat{\rho})|}. \tag{22}$$

As shown in Fig. 1, even for high values of the perturbation parameter ($K \gg K_c$) there are an infinite number of regions of Larmor radius values, for which KAM curves can be restored and chaos suppressed. The gyro-averaging operation “breaks” the critical line at the zeros of the zero-order Bessel function. In particular, near the zeros, the critical perturbation goes to infinity and the transition to global chaos cannot occur. Writing $\hat{\rho} = \rho_i + \delta\hat{\rho}$, where ρ_i is the i -th zero of J_0 and $\delta\hat{\rho} \ll 1$, and expanding in Taylor series, the divergence of the critical perturbation near the zeros of J_0 can be approximated as

$$K \approx \frac{K_c/|J_1(\rho_i)|}{|\hat{\rho} - \rho_i|}, \tag{23}$$

where J_1 denotes the Bessel function of first order. The first five positive zeros, indicated in Fig. 1, are approximately $\rho_1 = 2.40$, $\rho_2 = 5.52$, $\rho_3 = 8.65$, $\rho_4 = 11.79$, and $\rho_5 = 14.93$.

The effect of chaos suppression is illustrated by Figs. 2(a) and 2(b). Figure 2(a) shows a GSM Poincare section for $\hat{\rho} = 3.9$ and $K = 8.0$, which corresponds to the point P_0 in Fig. 1. No KAM curves are observed in the Poincare section as P_0 belongs to the region of global chaos. Keeping the same value of K and changing the value of $\hat{\rho}$ to ρ_2 (point P_1 in Fig. 1) eliminates all the chaotic orbits (see Figure 2(b)).

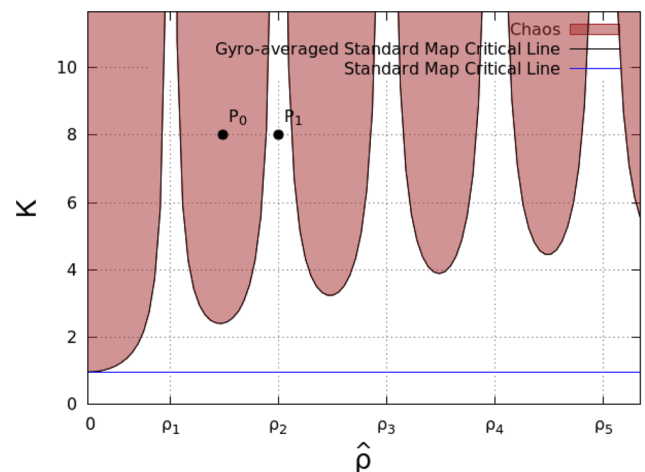


FIG. 1. Critical lines for the standard map (blue horizontal line) and for the gyro-averaged standard map (black curves). Inside the shaded regions there is global chaos.

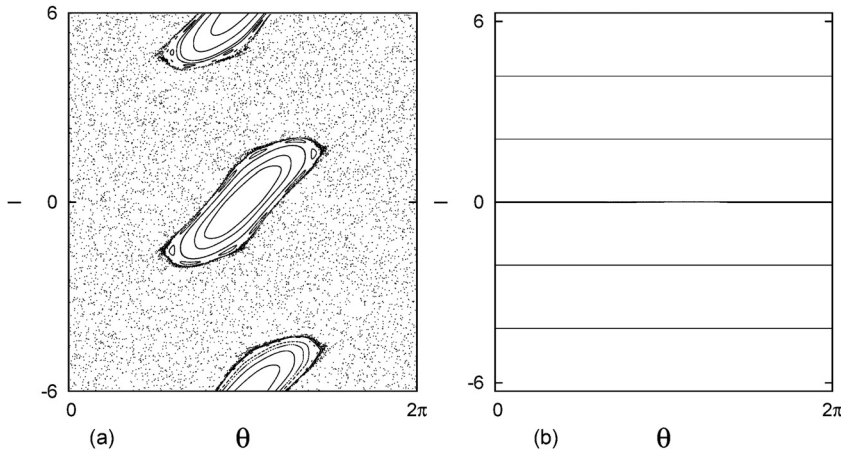


FIG. 2. (a) GSM Poincaré section for $\hat{\rho} = 3.9$ and $K = 8.0$ (point P_0 in Figure 1): No KAM curves are observed. (b) GSM Poincaré section for $\hat{\rho} = 5.52$ and $K = 8.0$ (point P_1 in Figure 1): KAM curves are restored.

IV. GYRO-AVERAGED STANDARD NONTWIST MAP (GSNM)

As a second example of the gyro-averaged drift wave map, we introduce the GSNM, which corresponds to a non-monotonic radial electric field. In this case, the equilibrium potential is

$$\phi_0(x) = \alpha \left[\left(\frac{x}{L} \right) - \frac{1}{3} \left(\frac{x}{L} \right)^3 \right], \quad (24)$$

where α and L are dimensional constants. The gyro-average of Eq. (24) gives

$$\langle H_0(x) \rangle_\phi = \frac{\alpha}{B_0} \left[\left(\frac{x}{L} \right) \left(1 - \frac{\rho^2}{2L^2} \right) - \frac{1}{3} \left(\frac{x}{L} \right)^3 \right], \quad (25)$$

and from Eq. (13), we get the non-monotonic parabolic frequency profile

$$\Omega(x) = \frac{\alpha}{B_0 L} \left\{ \left[1 - \left(\frac{\rho}{\sqrt{2}L} \right)^2 \right] - \left(\frac{x}{L} \right)^2 \right\}, \quad (26)$$

which has a maximum at $x = 0$. For $\rho = 0$, the zeros of $\Omega(x)$ (and also of the E_r profile) are located at $\pm L$, where L is the characteristic length of the frequency profile. Substituting Eq. (26) into Eq. (12), we obtain

$$x_{n+1} = x_n + \frac{2\pi}{\omega_0 B_0} A k J_0(k\rho) \sin(ky_n), \quad (27)$$

$$y_{n+1} = y_n + \frac{2\pi}{\omega_0 B_0 L} \alpha \left\{ \left[1 - \left(\frac{\rho}{\sqrt{2}L} \right)^2 \right] - \left(\frac{x_{n+1}}{L} \right)^2 \right\}. \quad (28)$$

Introducing the dimensionless variables

$$I = -\frac{x}{L}, \quad \theta = \frac{ky}{2\pi}, \quad (29)$$

we get the GSNM

$$I_{n+1} = I_n - b J_0(\hat{\rho}) \sin(2\pi\theta_n), \quad (30)$$

$$\theta_{n+1} = \theta_n + a \left[\left(1 - \frac{\bar{\rho}^2}{2} \right) - I_{n+1}^2 \right], \quad \text{mod } 1, \quad (31)$$

where

$$a = \frac{\alpha k}{\omega_0 B_0 L} \quad b = \frac{2\pi a A}{\alpha}, \quad (32)$$

$$\bar{\rho} = \frac{\rho}{L} \quad \hat{\rho} = k\rho \quad (33)$$

are four dimensionless parameters. We refer to b as the perturbation parameter, which is proportional to the amplitude A of the drift waves. Like in the GSM case, we can also define an effective perturbation parameter

$$b_{ef} = b J_0(\hat{\rho}). \quad (34)$$

As indicated in Eq. (33), $\bar{\rho}$ and $\hat{\rho}$ correspond to the Larmor radius normalized using two different length scales: the characteristic length of the frequency profile L and the wavelength $\lambda = \frac{2\pi}{k}$, respectively.

A. Fixed points

According to Eqs. (30) and (31), the fixed points of the GSNM, $I^* = I_{n+1} = I_n$ and $\theta^* = \theta_{n+1} = \theta_n$, satisfy

$$0 = b J_0(\hat{\rho}) \sin(2\pi\theta^*), \quad (35)$$

$$m = a \left[\left(1 - \frac{\bar{\rho}^2}{2} \right) - I^{*2} \right], \quad (36)$$

where m is an integer number. For each $m \in \mathbb{Z}$, $a \neq 0$, $b J_0(\hat{\rho}) \neq 0$, and $\bar{\rho} \leq \sqrt{2(1 - \frac{m}{a})}$, there are four fixed points

$$P_{\pm} = (0, \pm I_*(\bar{\rho})), \quad (37)$$

$$Q_{\pm} = \left(\frac{1}{2}, \pm I_*(\bar{\rho}) \right), \quad (38)$$

where

$$I_*(\bar{\rho}) = \frac{1}{\sqrt{2}} \sqrt{2 \left(1 - \frac{m}{a} \right) - \bar{\rho}^2}. \quad (39)$$

Note that the θ coordinate of P_{\pm} and Q_{\pm} does not depend on any parameters. If $\bar{\rho} = \sqrt{2(1 - \frac{m}{a})}$, the pair of points $\{P_+, P_-\}$ collide at $(0, 0)$, and $\{Q_+, Q_-\}$ collide at $(\frac{1}{2}, 0)$. Figure 3 shows the I -axis position of both pairs for $m = 0$ and

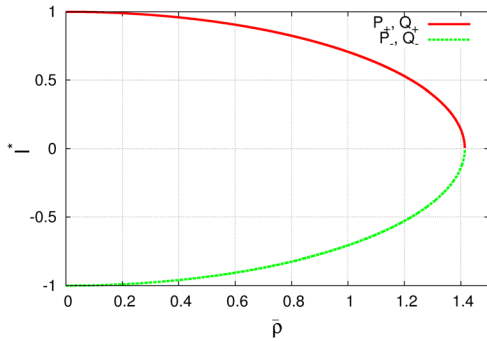


FIG. 3. Coordinate I of fixed points for $m=0$ and increasing $\bar{\rho}$. The fixed points collide at $\bar{\rho} = \sqrt{2}$ and do not exist for $\bar{\rho} > \sqrt{2}$.

increasing $\bar{\rho}$. The collision occurs for $\bar{\rho} = \sqrt{2}$. For higher values of $\bar{\rho}$, the fixed points do not exist.

The stability of a k -periodic orbit of a map M is determined by the residue

$$R = \frac{1}{4} \left[2 - \text{Tr} \left(\prod_{i=0}^{k-1} J(\bar{x}_i) \right) \right], \quad (40)$$

where J is the Jacobian matrix of M , evaluated at the k -periodic orbit $\{\bar{x}_i\}_{i=0}^{k-1}$. If $0 < R < 1$, the periodic orbit is elliptic (stable); if $R < 0$ or $R > 1$, it is hyperbolic (unstable); and it is parabolic for $R = 0$ or $R = 1$. Applying formula (40) to the GSNM fixed points in Eqs. (37) and (38), we get

$$R(P_{\pm}) = R(Q_{\mp}) = \mp \pi ab J_0(\hat{\rho}) I_*(\bar{\rho}). \quad (41)$$

The stability of the fixed points $\{P_{\pm}, Q_{\pm}\}$ with $m=0$ can be analyzed using the parameter $\Lambda(a, b, \hat{\rho}, \bar{\rho}) = R(P_-)$. As shown in Fig. 4, depending on the value of Λ , there are three possible configurations. The symbol “x” denotes a hyperbolic

point and “o” an elliptic point. The points have their stability inverted when $-1 < \Lambda < 0$ (configuration II), as indicated in Fig. 4(b). All the fixed points are hyperbolic in configuration III, Fig. 4(c), which occurs for $\Lambda < -1$ or $\Lambda > 1$.

B. Separatrix reconnection

The location and stability of the fixed points determine the different phase space topologies of the GSNM. These topologies, illustrated in Fig. 5, are characteristic of nontwist maps and are called heteroclinic, separatrix reconnection, and homoclinic.¹⁷ Since the Larmor radius changes the stability of the fixed points, it is expected that it will also change the topology. Figures 5(a)–5(c) show the heteroclinic-type, separatrix reconnection, and the homoclinic-type topologies in Poincaré sections of the GSNM for different values of a and b , and fixed values of $\hat{\rho}$ and $\bar{\rho}$.

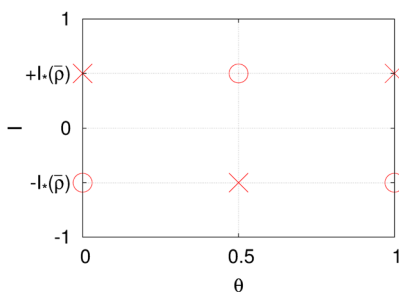
To determine the condition for separatrix reconnection associated to the fixed points P_{\pm} and Q_{\pm} with $m=0$, we follow Refs. 17 and 20 and approximate the GSNM in the vicinity of the fixed points by the Hamiltonian

$$H(I, \theta) = a \left[I \left(1 - \frac{\bar{\rho}^2}{2} \right) - \frac{I^3}{3} \right] - \frac{b}{2\pi} J_0(\hat{\rho}) \cos(2\pi\theta). \quad (42)$$

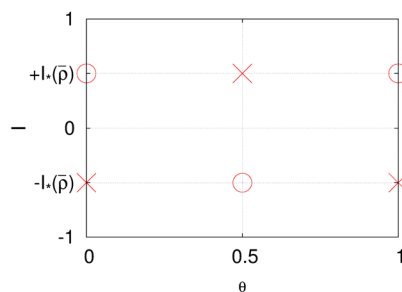
For $0 < \Lambda < 1$ (configuration I), separatrix reconnection occurs when $H(P_+) = H(Q_-)$. If $-1 < \Lambda < 0$ (configuration II), reconnection is observed when $H(P_-) = H(Q_+)$. Combining these two conditions, we obtain the reconnection condition

$$a = \frac{3}{4\pi} \sigma(\hat{\rho}, \bar{\rho}) b \quad (43)$$

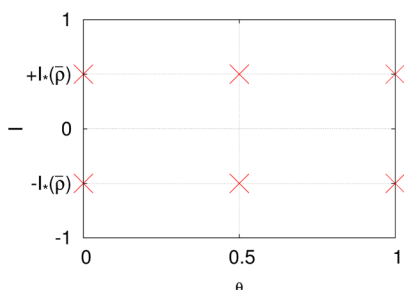
where



(a) Configuration I: $0 < \Lambda < 1$

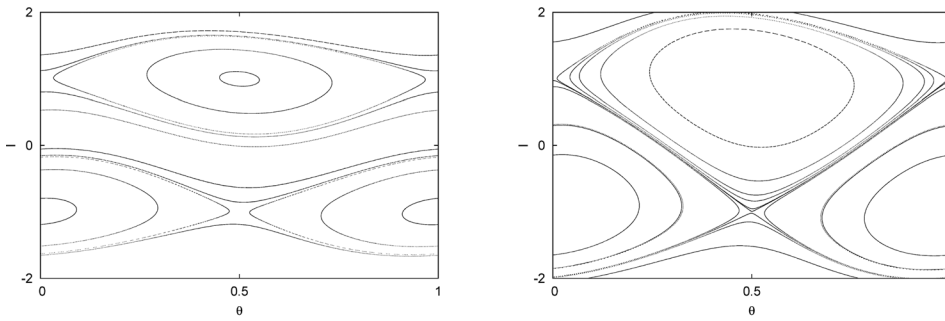


(b) Configuration II: $-1 < \Lambda < 0$



(c) Configuration III: $\Lambda < -1$ or $\Lambda > 1$.

FIG. 4. Stability of the fixed points P_{\pm} and Q_{\pm} with $m=0$.

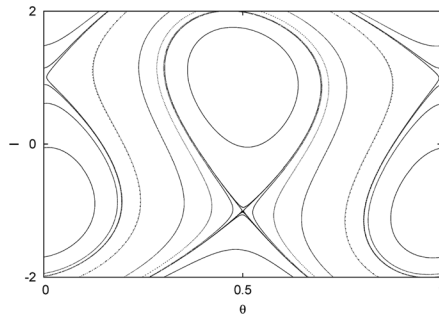


(a) Heteroclinic-type topology with

$$a = 0.0796 \text{ and } b = 0.125.$$

(b) Separatrix reconnection with

$$a = 0.0478 \text{ and } b = 0.2.$$



(c) Homoclinic-type topology with

$$a = 0.0239 \text{ and } b = 0.3.$$

$$\sigma(\hat{\rho}, \bar{\rho}) = \frac{|J_0(\hat{\rho})|}{\left(1 - \frac{\bar{\rho}^2}{2}\right)^{\frac{3}{2}}}. \quad (44)$$

The reconnection line divides the a - b parameter space in two regions: one with heteroclinic-type topology ($\frac{a}{b} > \frac{3}{4\pi} \sigma(\hat{\rho}, \bar{\rho})$) and another with homoclinic-type topology ($\frac{a}{b} < \frac{3}{4\pi} \sigma(\hat{\rho}, \bar{\rho})$). The slope of the reconnection line is defined by the angle $\arctan\left[\frac{3}{4\pi} \sigma(\hat{\rho}, \bar{\rho})\right]$. Figure 6 shows isolines of the angle $\arctan\left[\frac{3}{4\pi} \sigma(\hat{\rho}, \bar{\rho})\right]$. Keeping a and b fixed, the topology of the phase space remains unchanged, if the parameters $\hat{\rho}$ and $\bar{\rho}$ vary over an isoline. As an example, for a and b such that $a = \frac{3}{4\pi} b$ (which corresponds to the reconnection condition in the standard nontwist map¹⁷), there is reconnection for any values of $\hat{\rho}$ and $\bar{\rho}$ over the red isoline in Fig. 6. The red isoline crosses the point $\hat{\rho} = \bar{\rho} = 0$ where the GSNM reduces to the standard nontwist map. For high (red) values of σ , the slope of the reconnection line approaches $\frac{\pi}{2}$, and the phase space is characterized by the homoclinic-type topology for a fixed a and almost every value of the parameter b . For low (blue) values of σ , the slope of the reconnection line tends to 0, and the phase space is characterized by the heteroclinic-type topology for a fixed b and almost every value of the parameter a .

C. Nontwist transport barrier

The transition to global chaos in the GSNM corresponds to the destruction of the NTB, which is a robust non-chaotic

FIG. 5. GSNM phase space topologies associated with the fixed points P_{\pm} and Q_{\pm} with $m=0$. In all figures, the Larmor radius is such that $\hat{\rho} = 0.05$ and $\bar{\rho} = 0.01$.

region of KAM curves dividing the phase space. The NTB is robust in the sense that their KAM curves are typically more resilient to perturbation than other KAM curves in the system.

Consider the 3/2-degrees-of-freedom Hamiltonian system

$$H = H_0(I) + \epsilon V(I, \theta, t), \quad (45)$$

where I and θ are the action-angle variables of the integrable system, H_0 , and the parameter ϵ controls the strength of the time-periodic perturbation V . In this case, the twist (non-degeneracy) condition is

$$\frac{d\Omega}{dI} = \frac{d^2 H_0}{dI^2} \neq 0, \quad (46)$$

for all I . If there is at least one critical point for which $d\Omega/dI = 0$, the non-degeneracy condition is violated and the Hamiltonian in Eq. (45) is nontwist. One of the main properties of these systems is the presence of robust NTBs located at the critical points (maxima or minima) of the frequency profile even in the case when most of the phase space is chaotic.¹⁷ As discussed before, the GSNM can be obtained by integrating the equations of motion of the 3/2-degrees of freedom Hamiltonian in Eq. (8). This is a nontwist Hamiltonian because the frequency in Eq. (26) has a critical point at $x=0$. Figure 7 shows a Poincaré section of the GSNM with $a=0.354$, $\bar{\rho} = 0$, and $bJ_0(\hat{\rho}) = 0.8$. As

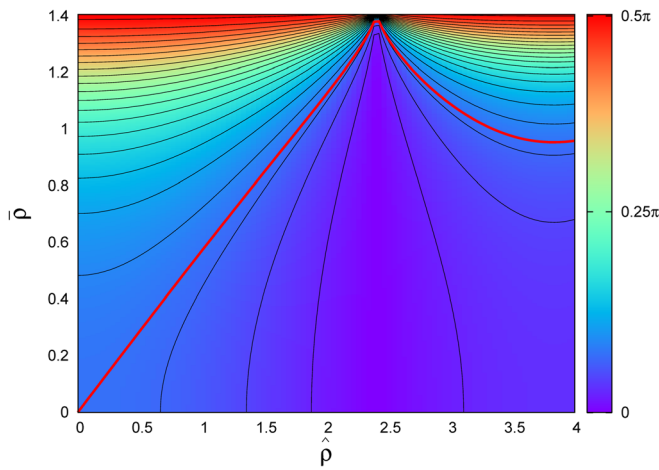


FIG. 6. Isolines of $\arctan[\frac{3}{4\pi}\sigma(\hat{\rho}, \bar{\rho})]$: varying $\hat{\rho}$ and $\bar{\rho}$ along isolines does not change the topology of the phase space. For high (red) values of σ , homoclinic-type is observed topology for a fixed a and almost every value of b . For low (blue) values of σ , heteroclinic-type topology is observed for a fixed b and almost every value of a .

expected, the phase space is characterized predominantly by chaotic orbits (green and red regions), but it has a robust NTB consisting of “belt” of KAM curves (black curves).

D. Breakup diagrams

Here, we study the transition to global chaos in the GSNM, i.e., the destruction of the robust KAM curves that constitute the NTB. It is important to remark that the transition to global chaos in nontwist systems is still an open problem. However, a possible approach to this problem consists of estimating the parameter values or the critical thresholds, which determine the breakup of the shearless KAM curve. In the absence of a perturbation, the shearless KAM curve is located where the twist condition is violated, and the parameter values for the destruction of the NTB can be estimated from the parameter values that determine the breakup of the shearless curve.

A standard way to determine the parameter values for the destruction of the shearless curve is based on the indicator point (IP) method proposed in Ref. 35 and used in several works including Refs. 6, 19, and 37. This method consists on finding the parameter values for which the iterations of the indicator point, which defines the indicator point orbit (IPO), are chaotic. If the IPO is quasiperiodic, it traces a shearless KAM curve. When the IPO is chaotic, the shearless curve is broken. In nontwist maps with special symmetries, like the ones studied here, the indicator points can be easily found by computing the fixed points of the reversing symmetry group transformations. Further details can be found in Ref. 36. Following a procedure similar to the one in Ref. 37, we obtained the following IPs for the gyro-averaged standard nontwist map

$$z_0^1 = \left(\frac{1}{4}, \frac{bJ_0(\hat{\rho})}{2}\right) \quad z_0^2 = \left(\frac{3}{4}, -\frac{bJ_0(\hat{\rho})}{2}\right), \quad (47)$$

$$z_1^1 = \left(\frac{a}{2} \left[1 - \frac{\bar{\rho}^2}{2}\right] + \frac{1}{4} \pmod{1}, 0\right) \quad (48)$$

$$z_1^2 = \left(\frac{a}{2} \left[1 - \frac{\bar{\rho}^2}{2}\right] + \frac{3}{4} \pmod{1}, 0\right).$$

Once the IPs are found, the next step is to obtain the critical thresholds using an appropriate criterion to determine if the IPO is chaotic. Our criterion is based on the technique proposed in Ref. 26, which considers the recurrence properties of the IPO in conjunction with Slater’s Theorem.³⁸ Recurrence properties and their relation to the Slater’s Theorem were also discussed in Ref. 27. In Ref. 28, the technique described in Ref. 26 was used to study the breakup of the shearless curve in the nontwist standard map. The Slater’s Theorem states that for any quasiperiodic motion on the circle, there are at most three different recurrences, or return times, in any connected interval. Although this theorem was originally formulated for circle maps, it can also be applied to two-dimensional systems, once the dynamics on a KAM curve is mapped to a quasiperiodic rotation on a circle.²⁶ The recurrence time is defined as the number of iterations that an orbit takes to return to a neighborhood of a point. Our procedure to characterize the dynamics of an indicator point orbit of the GSNM is the following: with any one of the indicator points as the initial condition, we compute the orbit for N iterations and choose the point of the orbit which has the maximum number of different recurrence times. If there are more than three different recurrence times, we conclude that the orbit is chaotic and the corresponding KAM curve is destroyed. More precisely, the procedure consists of the following steps:

- Compute the orbit $O = \{u_k\}_{k=0}^N$ with initial condition $u_0 = z_1^1$, where N is the number of iterations.
- Construct the recurrence matrix:⁴⁰

$$R_{ij} = \Theta(\epsilon - \|u_i - u_j\|), \quad (49)$$

where $i, j \in \{0, \dots, N\}$, $u_i, u_j \in O$, Θ is the Heaviside function, and ϵ is a parameter defining the size of the neighborhood. If the distance between u_i and u_j , given by the norm $\|u_i - u_j\|$, is less than ϵ , $R_{ij} = 1$; otherwise, $R_{ij} = 0$.

- Define the recurrence time as $\tau_{ij} = |i - j|$ for $i \neq j$ and $R_{ij} = 1$. That is, the recurrence time is τ_{ij} if the orbit crosses the neighborhood of u_j at the i -th iteration. For each point u_j , compute the set of different recurrences $S_R^{(j)} = \cup_{i=0, i \neq j}^N \{\tau_{ij}\}$.
- Determine the maximum number of different recurrence times

$$n_R = \max\{n(S_R^{(j)})\}_{j=0}^N, \quad (50)$$

where n is the number of recurrence times belonging to $S_R^{(j)}$, and use the Slater’s Theorem to conclude that the orbit O is chaotic if $n_R > 3$.

For $n_R \leq 3$, the characterization of the dynamics using the Slater’s Theorem is inconclusive because the orbit might be periodic, quasiperiodic, or even chaotic. In this case, the number of iterations, N , can be increased to explore if n_R

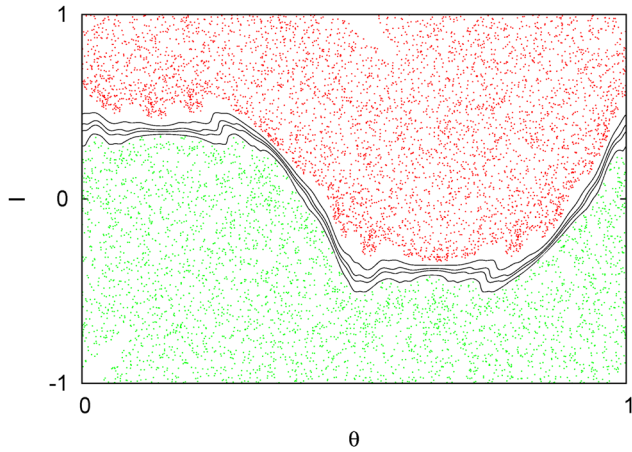


FIG. 7. Nontwist transport barrier in the GSNM: robust region of KAM curves (black curves) splitting the phase space in two chaotic regions, indicated by the red and green orbits.

increases beyond three. If the condition $n_R \leq 3$ still persists and no change in n_R is observed, the orbit is deemed periodic if $n_R=1$ and quasiperiodic if $n_R=3$. The case $n_R=2$ requires a more careful analysis with higher values N . Increasing N , n_R stabilizes in 3, indicating quasiperiodic dynamics, or assumes values greater than 3, which is the case for chaotic dynamics. Although rigorous criteria for the case $n_R \leq 3$ are lacking, the numerical results in Refs. 26 and 27 support the use of recurrences in conjunction with Slater's theorem as a computationally efficient diagnostic to identify chaotic orbits.

We now apply this diagnostic to compute breakup diagrams for the GSNM showing regions in parameter space where the shearless curve is broken. The diagrams were constructed by computing the recurrences of IPOs for $\epsilon=0.1$, and two different number of iterations, $N=100$ and $N=1000$. Since the GSNM has four free parameters, only two parameters were varied at a time while the others were kept constant. Our first example is presented in Fig. 8, where we fixed $a=0.1$, $\bar{\rho}=0$ (which corresponds to the limit $\rho \ll$

L), and plotted the values of n_R on a 1000×1000 grid in the $(\hat{\rho}, b)$ space. The main difference between $N=100$ and $N=1000$ is observed in points with $n_R=2$, but even for a relatively small number of iterations it is possible to identify the breakup of the shearless curve in domains where $n_R > 3$. These domains have points plotted with magenta, red, and yellow colors. Green points ($n_R=3$) are concentrated in domains with low effective perturbation b_{ef} , which means small b or $\hat{\rho}$ close to a zero of the zero-order Bessel function. For parameter values outside the green region (e.g., points A and C in Fig. 8), the IPO is chaotic, and, as shown in Fig. 9, the shearless curve is destroyed. For $\hat{\rho}$ values near a zero of J_0 (e.g., point B of Fig. 8), the shearless KAM curve is restored, as shown by the red orbit in Fig. 9.

Breakup diagrams with varying a and $\hat{\rho}$ are shown in Fig. 10. The number of iterations used to construct the first diagram was $N=100$. In the second diagram, the number of iterations was increased to $N=1000$. As before, regions where $n_R=3$, which are indicators of non-chaotic dynamics, are concentrated near the zeros of J_0 . A high occurrence of points with $n_R=3$ is also observed in regions with low a . When the number of iterations is increased from $N=100$ to $N=1000$, it is observed that the main geometric features remain the same, although several points with $n_R=1$ and $n_R=2$ transition to $n_R > 3$. Poincare sections for parameters corresponding to points A, B, and C in Fig. 10 are showed in Figs. 11(a)–11(c). As expected, the shearless KAM curve is broken at points A and C, and restored at point B.

Additional examples of breakup diagrams are presented in Figs. 12(a)–12(d). The parameters are the same as those in Figs. 8(b) and 10(b), but the value of the fixed parameter $\bar{\rho}$ is higher. Comparing Figs. 12(a) and 12(b) with Fig. 8(b), it is observed that increasing $\bar{\rho}$ leads to an increase in the number of points with $n_R=3$ and to the robustness of the shearless KAM curve. As shown in Figs. 12(c) and 12(d), the distribution of points with $n_R=3$ changes when $\bar{\rho}$ increases, resulting in different critical thresholds but with no significant suppression of green points. Red and yellow points disappear

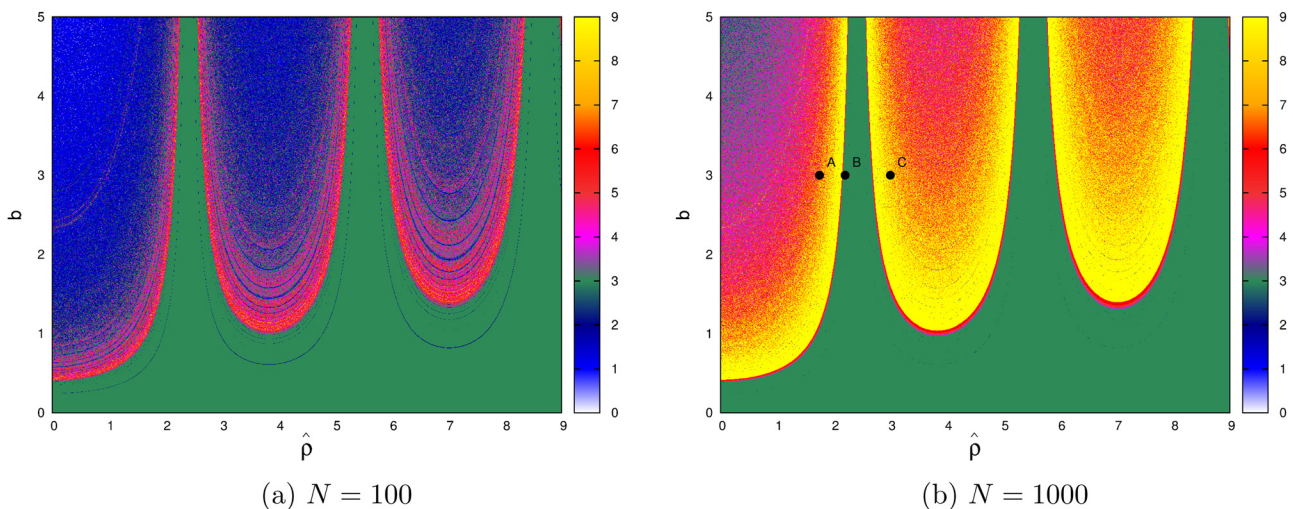


FIG. 8. GSNM breakup diagrams for $\hat{\rho}$ versus b , with $\bar{\rho}=0$ and $a=0.1$. For each point $(\hat{\rho}, b)$ in the diagram, the IPO and the corresponding n_R are computed with $\epsilon=0.1$. The color pallet indicates the value of n_R . The breakup of the shearless curve can be detected in the points where $n_R > 3$. The IPO is quasiperiodic in the green region ($n_R=3$), which corresponds to low effective perturbation b_{ef} , i.e., low b or $\hat{\rho}$ near a zero of J_0 .

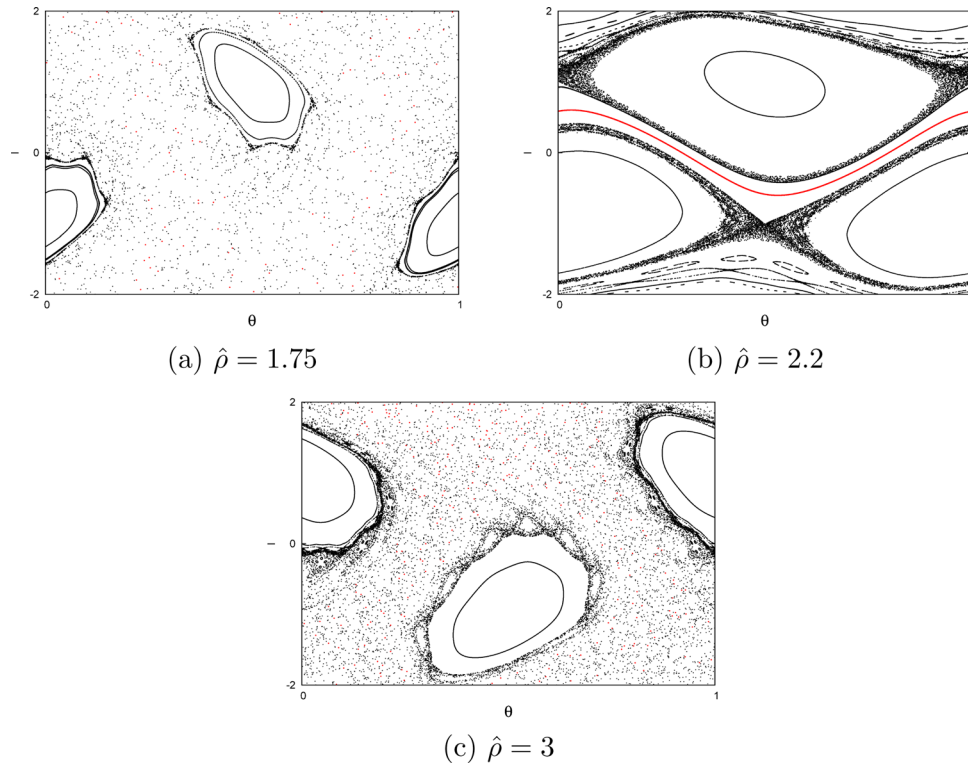


FIG. 9. Restoration of shearless KAM curve (identified through a quasiperiodic IPO shown in red) for $\hat{\rho}$ values near the zeros of J_0 and $a=0.1$, $b=3$, and $\bar{\rho} = 0$. Panels (a), (b), and (c) correspond to parameter values A, B, and C indicated in Fig. 8. As expected, for $\hat{\rho} = 2.2$, which is near a zero of the Bessel function, the effective perturbation parameter is small and the shearless curve is restored.

in certain regions and reappear in others, as can be seen by comparing Figs. 10(b), 12(c), and 12(d).

Summarizing, in this section, we used a computational technique based on the recurrence properties of the IPO to estimate the critical parameter values for the breakup of the shearless KAM curve. In particular, we computed breakup diagrams to understand the role of finite Larmor radius effects on the destruction and formation of shearless KAM curves. It was observed that when $\hat{\rho}$ is close to a zero of J_0 , the shearless curve becomes more robust to perturbation in b . This is because, near the zeros of J_0 , the GSNM's Hamiltonian is effectively integrable. In particular, as $\hat{\rho}$ approaches a zero of J_0 , the shearless curve and the KAM curves that make up the nontwist transport barrier are restored. The robustness of the shearless curve and the critical thresholds are also modified by increasing $\bar{\rho}$.

V. GYRO-AVERAGED QUARTIC NONTWIST MAP (GQNM)

In this section, we propose another area-preserving map, the GQNM. A key property of the GQNM is that it exhibits a zonal flow bifurcation similar to the one observed in the nontwist Hamiltonian system of Ref. 6. The Hamiltonian system in Ref. 6 is a drift-wave model of the $\mathbf{E} \times \mathbf{B}$ transport with FLR effects, and the zonal flow bifurcation corresponds to a bifurcation of the maximum of the $\mathbf{E} \times \mathbf{B}$ zonal flow velocity when the Larmor radius increases.

As in the previous maps, the GQNM is obtained from the gyro-averaged drift wave map in Eqs. (11) and (12). The equilibrium potential is similar to the one proposed in Ref. 6

$$\phi_0(x) = \alpha \tanh\left(\frac{x}{L}\right), \quad (51)$$

where α and L are dimensional constants. Applying the gyro-average operation (4) to (51) gives

$$\langle H_0(x) \rangle_\varphi = \frac{\alpha}{2\pi B_0} \int_0^{2\pi} \tanh\left(\frac{x}{L} + \frac{\rho}{L} \cos \varphi\right) d\varphi, \quad (52)$$

and from Eq. (13), we get the nonlinear frequency

$$\Omega(I) = \frac{\alpha}{2\pi L B_0} \int_0^{2\pi} \text{sech}^2(I + \bar{\rho} \cos \varphi) d\varphi, \quad (53)$$

where $I = x/L$ and $\bar{\rho} = \rho/L$. The zonal flow bifurcation results from a bifurcation of the critical point of the frequency profile. To analyze it in a simple setting, consider the Taylor series approximation of (53) for small values of $|I|$ and $\bar{\rho}$

$$\Omega(I) \approx \frac{\alpha}{L B_0} (1 - I^2) \left\{ 1 - \bar{\rho}^2 \left[\frac{3}{2} (1 - I^2) - 1 \right] \right\}. \quad (54)$$

Figure 13 shows the frequency profile in Eq. (54) for different values of $\bar{\rho}$. For $\bar{\rho} = 0$, there is only one critical point, $\Omega' = 0$, which corresponds to a maximum at $I = 0$. Increasing $\bar{\rho}$ leads to an increase of the profile's "flatness" and eventually to a transition in which the maximum bifurcates into a minimum and two maxima. The bifurcation threshold $\bar{\rho}_b$ can be determined from the condition

$$\frac{\partial^2 \Omega}{\partial I^2} \Big|_{I=0, \bar{\rho}=\bar{\rho}_b} = 0, \quad (55)$$

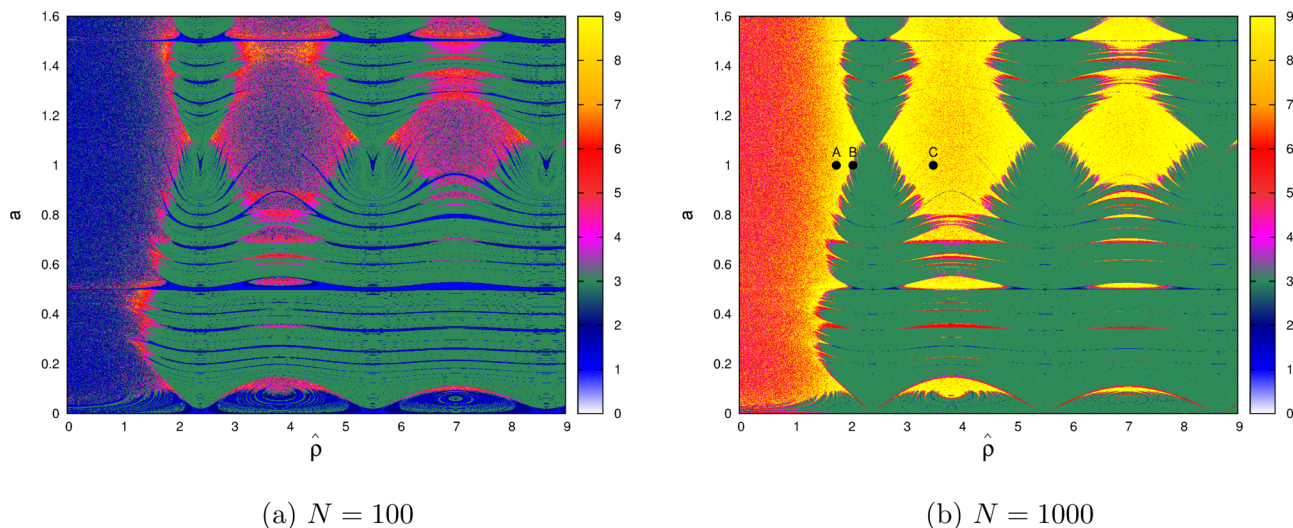


FIG. 10. GSNM breakup diagrams for $\hat{\rho}$ versus a , with $\bar{\rho} = 0$ and $b = 1.5$. Neighborhood size: $\epsilon = 0.1$. Green points, corresponding to quasiperiodic dynamics, are concentrated near the zeros of J_0 and in domains with low a .

which for Eq. (54) gives

$$\bar{\rho}_b = 1/\sqrt{2}. \tag{56}$$

Defining $I_n = x_n/L$, $\theta_n = ky_n/2\pi$, and $\hat{\rho} = k\rho$, and using Eq. (54), we get from Eqs. (11) and (12), the GQNM

$$I_{n+1} = I_n + bJ_0(\hat{\rho}) \sin(2\pi\theta_n), \tag{57}$$

$$\theta_{n+1} = \theta_n + a \left(1 - I_{n+1}^2 \right) \times \left\{ 1 - \bar{\rho}^2 \left[\frac{3}{2} (1 - I_{n+1}^2) - 1 \right] \right\}, \text{ mod } 1, \tag{58}$$

where $a = k\alpha/\omega_0LB_0$, and the perturbation parameter is $b = 2\pi aA/\alpha$. As in the previous maps, an effective perturbation parameter can be defined as $b_{ef} = bJ_0(\hat{\rho})$. Like the GSNM, the GQNM reduces to the standard nontwist map for

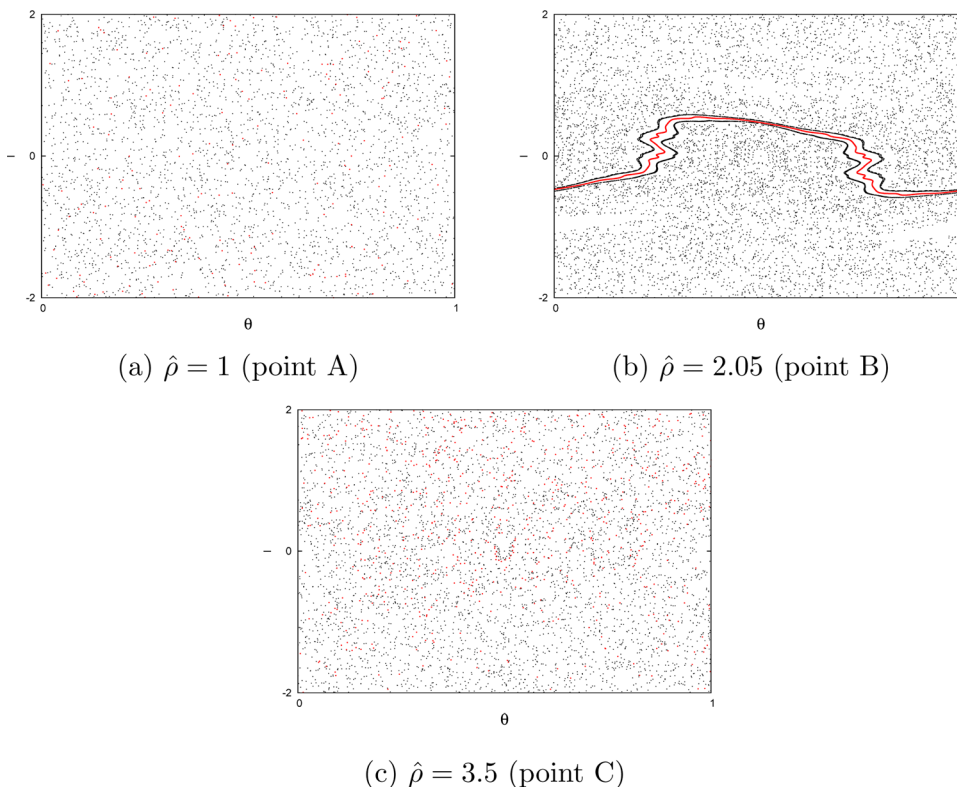


FIG. 11. Poincaré sections of the GSNM map for parameter values corresponding to points A, B, and C, in Fig. 8, and $a = 1$; $b = 1.5$; $\bar{\rho} = 0$. Consistent with Fig. 8(b), the shearless curve is restored for $\hat{\rho} = 2.05$.

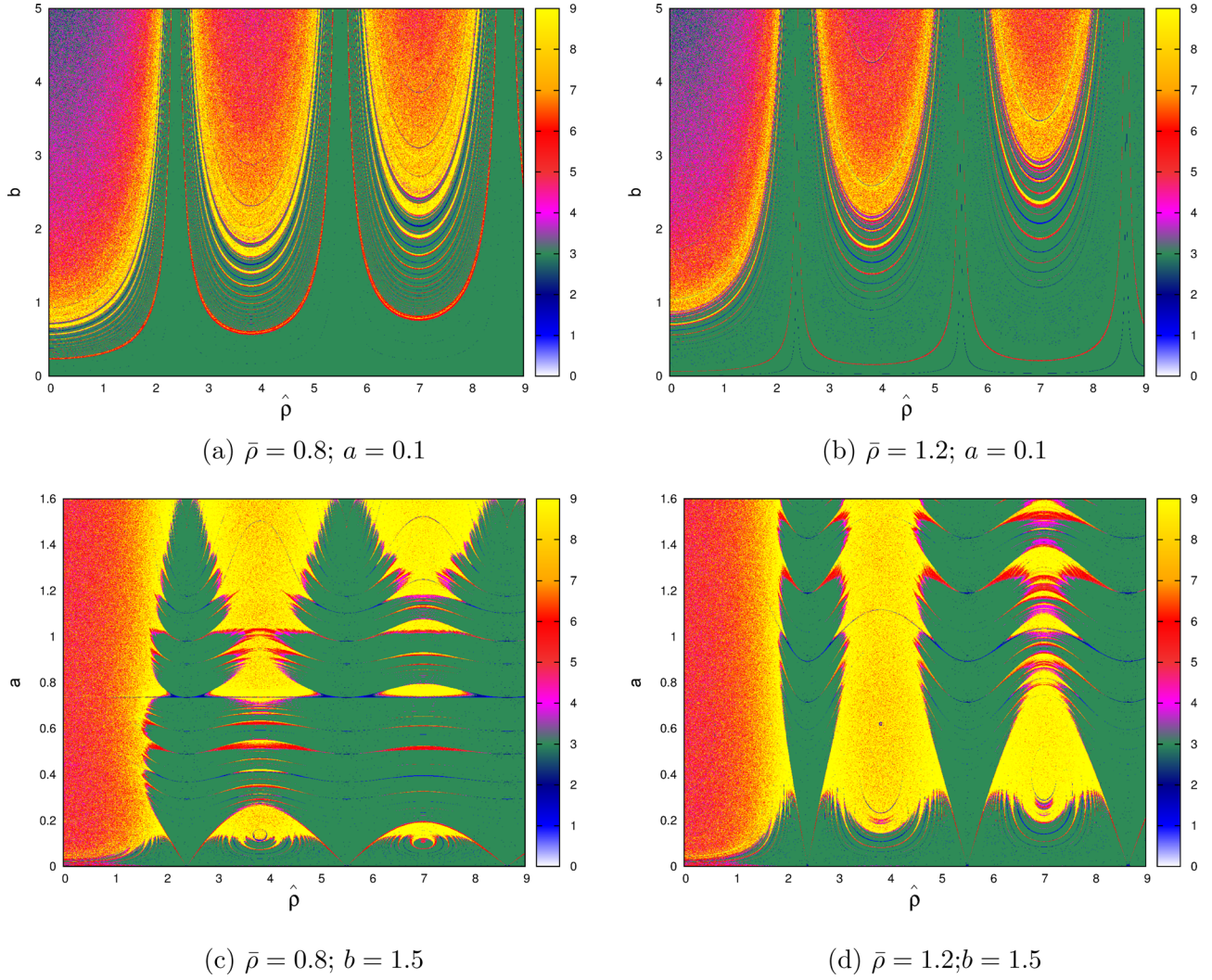


FIG. 12. Dependence of robustness of shearless curve on $\bar{\rho}$. As shown in (a) and (b), the robustness of the shearless KAM increases when $\bar{\rho}$ increases with fixed $a=0.1$. On the other hand, as shown in (c) and (d), a different behavior is observed for fixed $b=1.5$. In all diagrams, $N=1000$ and $\epsilon=0.1$.

$\hat{\rho} = \bar{\rho} = 0$. In what follows, we discuss FLR effects on the GQNM's fixed points and nontwist transport barriers.

A. Fixed points and nontwist transport barriers

The fixed points (θ^*, I^*) of the GQNM satisfy

$$0 = bJ_0(\hat{\rho}) \sin(2\pi\theta^*), \quad (59)$$

$$m = a(1 - I^{*2}) \left\{ 1 - \bar{\rho}^2 \left[\frac{3}{2}(1 - I^{*2}) - 1 \right] \right\}, \quad m \in \mathbb{Z}. \quad (60)$$

For $m=0$, $a \neq 0$, and $bJ_0(\hat{\rho}) \neq 0$, there are four fixed points independently of the value of $\hat{\rho}$

$$P_1^\pm = (0, \pm 1), \quad Q_1^\pm = \left(\frac{1}{2}, \pm 1 \right). \quad (61)$$

If $\bar{\rho} \geq 2\bar{\rho}_b = \sqrt{2}$, there is an additional set of fixed points

$$P_2^\pm = (0, \pm h(\bar{\rho})) \quad Q_2^\pm = \left(\frac{1}{2}, \pm h(\bar{\rho}) \right), \quad (62)$$

where

$$h(\bar{\rho}) = \sqrt{\frac{\bar{\rho}^2 - 2}{3\bar{\rho}^2}}. \quad (63)$$

Figure 14 shows the I coordinates of the fixed points with $m=0$. P_1^\pm and Q_1^\pm exist for all $\bar{\rho} \geq 0$ and are always located at $I = \pm 1$. P_2^\pm and Q_2^\pm only exist for $\bar{\rho} \geq 2\bar{\rho}_b = \sqrt{2}$ and their positions in the I axis are determined by the function $h(\bar{\rho})$, which satisfies $0 \leq h(\bar{\rho}) < \frac{1}{\sqrt{3}}$. The stability of the fixed points $\{P_1^\pm, Q_1^\pm, P_2^\pm, Q_2^\pm\}$ can be analyzed by evaluating the Green's residue in Eq. (40)

$$R(P_1^\pm) = -R(Q_1^\pm) = \mp \Lambda(a, b, \hat{\rho}, \bar{\rho}), \quad (64)$$

$$R(P_2^\pm) = -R(Q_2^\pm) = \pm h(\bar{\rho}) \Lambda(a, b, \hat{\rho}, \bar{\rho}), \quad (65)$$

where

$$\Lambda = \pi ab J_0(\hat{\rho})(1 + \bar{\rho}^2). \quad (66)$$

As shown in Fig. 15, depending on the value of Λ , there are five possible stability configurations. The number of elliptic fixed points reduces when Λ increases, and for $|\Lambda| > \frac{1}{h(\bar{\rho})}$, all the fixed points are hyperbolic. In general, the first points to

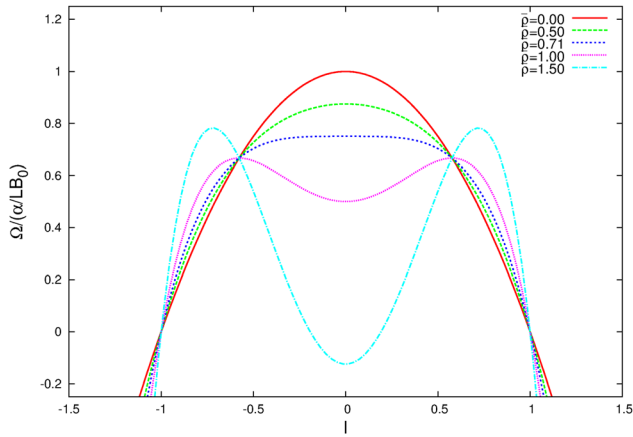


FIG. 13. Bifurcation of critical points in the frequency profile (54).

lose stability are the outer ones. Note that as $\bar{\rho}$ approaches $2\hat{\rho}_b$, $1/h(\bar{\rho})$ diverges, and the range of the configurations III and IV increases.

An important consequence of the zonal flow bifurcation is the occurrence of nontwist barrier bifurcations. In particular, for $\bar{\rho} \lesssim \bar{\rho}_b$, only one region with robust KAM curves is present (Fig. 16(a)), but for $\bar{\rho} > \bar{\rho}_b$ (Fig. 16(b)) two

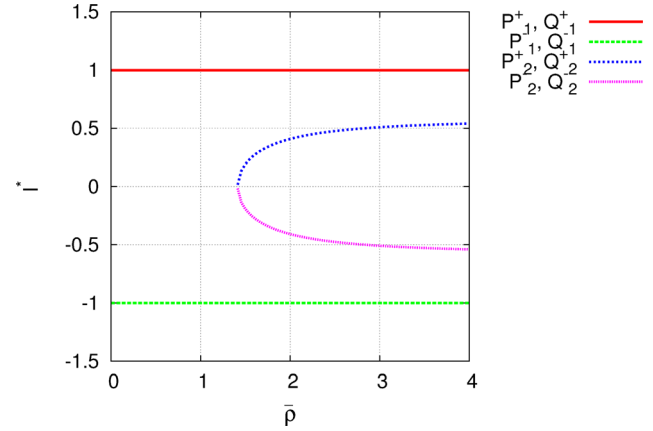


FIG. 14. I coordinates of fixed points with $m=0$ as function of $\hat{\rho}$. The set $\{P_1^\pm, Q_1^\pm\}$ exists for all values of $\bar{\rho}$. The set $\{P_2^\pm, Q_2^\pm\}$ only exists for $\bar{\rho} \geq 2\bar{\rho}_b = \sqrt{2}$.

additional NTBs appear. The outer NTBs are separated from the central one by two regions of confined chaotic orbits.

B. Robustness of the central shearless curve

Our interest in studying the robustness of KAM curves as function of b resides on the fact that this parameter is

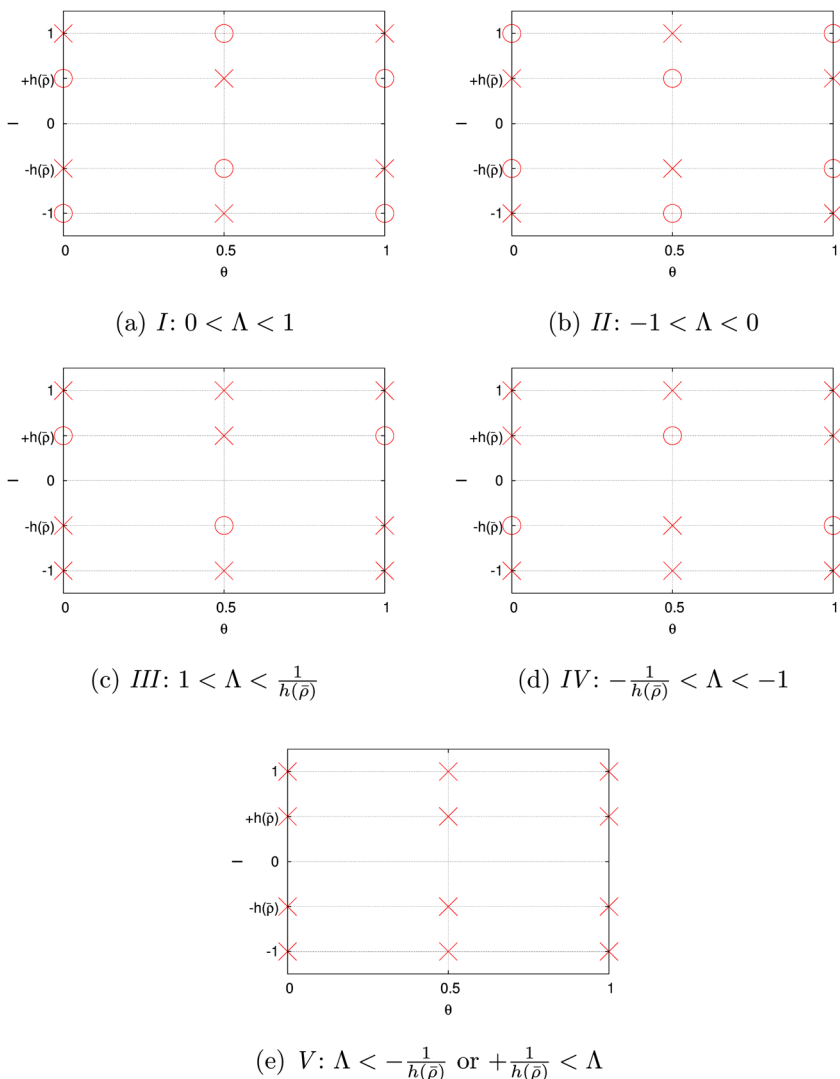


FIG. 15. Depending on the value of Λ , there are five possible configurations characterizing the stability of the period-one fixed points $\{P_1^\pm, Q_1^\pm, P_2^\pm, Q_2^\pm\}$ in the GQNM.

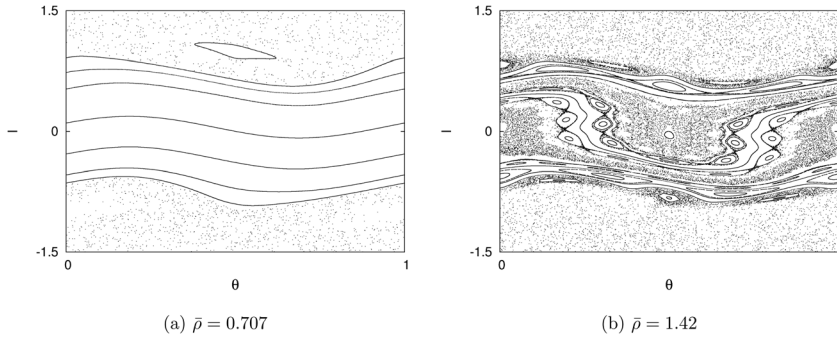


FIG. 16. (a) One NTB for $\bar{\rho} \lesssim \bar{\rho}_b$. (b) After the zonal flow bifurcation, three NTBs can be observed. Parameters: $a = 0.5$; $b = 1.35$; $\hat{\rho} = 2.8$.

proportional to the amplitude of the drift waves. For very small Larmor radius (or in the absence of FLR corrections), high amplitude values can easily destroy all KAM curves. However, this is not always the case when FLR effects are taken into account. In particular, like in the GSNM (see Sec. IV C), the robustness of the GQNM's shearless curve is significantly increased for $\hat{\rho}$ near a zero of J_0 .

Figures 17(a)–17(d) show breakup diagrams for the shearless KAM curve in the GQNM as function of b and $\bar{\rho}$.

In all cases, b_{ef} is small, because the values of $\hat{\rho}$ are close to the zeros of J_0 . Under this condition, and when $\bar{\rho}$ is close to the zonal flow bifurcation threshold $\bar{\rho}_b$ in Eq. (56), a significant increasing of the robustness of the shearless curve is observed. For $\bar{\rho} < \bar{\rho}_b$, higher values of b are required for breakup as $\bar{\rho}$ approaches $\bar{\rho}_b$, and for $\bar{\rho} > \bar{\rho}_b$, the robustness is reduced as $\bar{\rho}$ increases. That is, the robustness of the central NTB increases for $\hat{\rho}$ close to the zeros of J_0 , and for $\bar{\rho}$ close to $\bar{\rho}_b$.

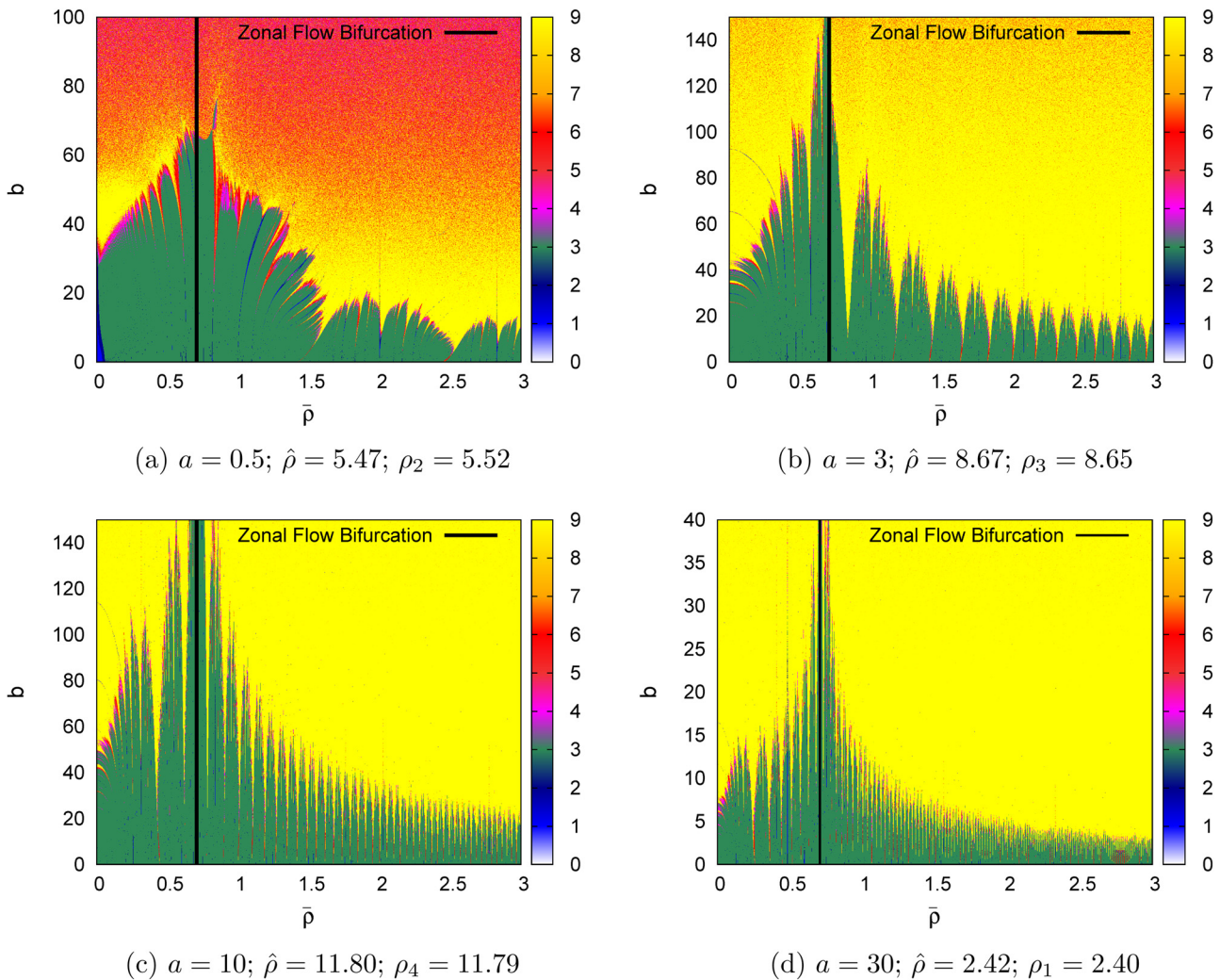


FIG. 17. For small b_{ef} values, the robustness of the central shearless curve (and, thus, also of the central NTB) increases with the degree of flatness of the frequency's profile around the critical point. The flatness can be controlled by the parameter $\bar{\rho}$ and becomes higher when $\bar{\rho}$ is close to the zonal flow bifurcation threshold $\bar{\rho}_b$ (shown with the solid black vertical line). The values of b_{ef} are made small by setting $\hat{\rho}$ close to the zeros of J_0 . The first four positive zeros are approximately given by: $\rho_1 = 2.40$; $\rho_2 = 5.52$; $\rho_3 = 8.65$; and $\rho_4 = 11.79$.

It is interesting to note that in the neighborhood of the $I=0$ shearless point, the degree of “flatness” of the frequency’s profile has a similar behavior. In particular, like the robustness of the central shearless curve, the degree of “flatness” (measured by $|\Omega''(0)|$) is higher near the bifurcation threshold, but it becomes smaller elsewhere. These results provide support to the conclusion that the robustness of NTBs in nontwist maps depends on the flatness of the frequency profile at the maximum or minimum (critical points), and that for small perturbation, the robustness increases with the degree of flatness.

The understanding of the role of the shear and the flatness of the frequency on the robustness of KAM curves is still an open problem. Among the first works addressing the role of shear is Ref. 39 where it was analytically and numerically shown that high shear reduces the strength of the perturbation required to break KAM surfaces. However, this work limited attention to monotonic frequencies with non-vanishing shear (i.e., twist systems) and did not address the breakup of shearless KAM curves. The robustness of NTBs is also related to the strong KAM stability in nontwist maps.²¹ According to the resonant overlap criterion,³¹ tori located between resonances break when the resonances overlap. Thus, one expects tori to be more resilient when the resonances’ widths are small. As shown in Ref. 21, in 3/2-degrees-of-freedom nontwist Hamiltonian systems, the width, $\delta\Omega$, of second-order degenerate resonances scales as

$$\delta\Omega \sim [\epsilon|\Omega''(I_0)|]^{2/3}, \quad (67)$$

where ϵ is the amplitude of the perturbation, and I_0 is such that

$$\Omega'(I_0) = 0 \quad \Omega''(I_0) \neq 0, \quad (68)$$

which according to Eq. (46) corresponds to the point where the twist condition is violated. When the system is slightly perturbed, second-order degenerate resonances appear in the neighborhood of the shearless curve, and their overlap leads to the break up of the shearless curve.

The central shearless curve of the GQNM is associated to the critical point $I_0=0$, where the frequency in Eq. (54) satisfies (68) for $\bar{\rho} \neq \bar{\rho}_b$. Thus, in the Hamiltonian system from which the GQNM is derived, second-order degenerate resonances might appear near the central shearless curve, and according to Eqs. (67) and (55), the width of these resonances scales as

$$\lim_{\bar{\rho} \rightarrow \bar{\rho}_b} \delta\Omega = 0 \quad (69)$$

because $|\Omega''(I_0)|$ vanishes for $\bar{\rho} = \bar{\rho}_b$. Small values of $|\Omega''(I_0)|$ result in small degenerate resonance widths and a more robust central shearless curve. As $|\Omega''(I_0)|$ is directly related to the flatness of the frequency’s profile at I_0 , Eq. (67) is consistent with the results of Figs. 17(a) and 17(d) and supports the conjecture relating the robustness of shearless curves to the flatness of the frequency at the degenerate points. Similar arguments can be applied to interpret the results in Ref. 16 where a study of the effect of the flatness of the q -profile on the robustness of NTBs was presented.

VI. SUMMARY AND CONCLUSIONS

In this paper, we studied finite Larmor radius effects on discrete models of $\vec{E} \times \vec{B}$ chaotic transport of test charged particles. The models are area-preserving Hamiltonian maps that assume an electrostatic potential consisting of the superposition of an equilibrium radial electrostatic field and a perturbation with a broad spectrum of drift waves. FLR effects were included by gyro-averaging the electrostatic potential and the maps were constructed from the integration of the resulting gyro-averaged $\vec{E} \times \vec{B}$ Hamiltonian system.

We constructed and studied three maps: the GSM, the GSNM, and the GQNM. In the GSM, the frequency, i.e., the gyro-averaged $\vec{E} \times \vec{B}$ zonal flow velocity, has a monotonic radial profile and the map satisfies the twist condition. In the GSNM and GQNM cases, the frequency is non-monotonic and as a result the maps are nontwist. Non-monotonic frequencies have degenerate points (i.e., points where the frequency is maximum or minimum), and in the vicinity of these points robust NTBs tend to form.

Typically, in area preserving maps, increasing the perturbation increases the chaos in the phase space. However, even for large perturbations, FLR effects can suppress chaos and restore broken KAM curves. The breakup diagrams provide the critical thresholds for the breakup of the shearless curve, which is one of the robust KAM curves that constitute the NTB. To determine the breakup of the shearless curve we used an efficient and accurate method based on the maximum number of different recurrence times. We showed that a relatively low number of iterations are sufficient to determine the main features of the breakup diagrams. Although, in general, chaos is suppressed when the Larmor radius is close to zeros of the zero-order Bessel function, the breakup diagrams exhibit a highly nontrivial fractal-like dependence on the Larmor radius and the other parameters of the map.

We also studied the role of the Larmor radius on the topology of the phase space and on bifurcations of the $\mathbf{E} \times \mathbf{B}$ zonal flow. In particular, we showed that the GSNM exhibits FLR dependent separatrix reconnection and obtained a formula determining the threshold for bifurcation from homoclinic to heteroclinic topologies as function of the Larmor radius. We also found that in the GQNM there is a critical value of the Larmor radius for which the maximum of the $\mathbf{E} \times \mathbf{B}$ zonal flow bifurcates into a minimum and two maxima. These zonal flow bifurcations create additional shearless curves that play a highly nontrivial role on transport.

Motivated by the key role that periodic orbits play on transport, we presented a detailed study of FLR effects on the location and stability of period-one orbits. In the GSNM, there are four period-one orbits and depending on the value of the Larmor radius, there are three possible stability configurations. In the GQNM, the situation is more complex due to the existence of zonal flow bifurcations. In particular, there can be up to eight period-one fixed points, four of which only exist for Larmor radii greater than a critical threshold. In this case, depending on the value of the Larmor radius, there are five stability configurations. It was found that the elliptic fixed points created by varying the Larmor radius are

strongly stable. The presence of elliptic points results in the formation of islands that can trap orbits in the phase space.

An important consequence of zonal flow bifurcations is the occurrence of up to three nontwist transport barriers. We focused on the central NTB and analyzed the robustness of the shearless curve using breakup diagrams. The results showed that the robustness of the central shearless curve significantly increases when the Larmor radius is close to the critical threshold for the zonal flow bifurcation. Based on this, we argued that in agreement with previous works the “flatness” of the frequency profile at the critical point is directly associated with the robustness of the central shearless curve.

ACKNOWLEDGMENTS

This work was made possible through financial support from the Brazilian research agency FAPESP under Grant No. 2013/00483-1. The authors would like to acknowledge Celso V. Abud for valuable discussions. DdCN was sponsored by the Office of Fusion Energy Sciences of the U.S. Department of Energy at Oak Ridge National Laboratory, managed by UT-Battelle, LLC, for the U.S. Department of Energy under Contract No. DE-AC05-00OR22725. J.D.F. gratefully acknowledges the hospitality of the Oak Ridge National Laboratory where part of the work was conducted.

¹R. G. Kleva and J. F. Drake, *Phys. Fluids* **27**, 1686 (1984).

²M. Pettini, A. Vulpiani, *et al.*, *Phys. Rev. A* **38**, 344 (1988).

³F. A. Marcus, I. L. Caldas, Z. O. Guimaraes Filho, P. J. Morrison, W. Horton, Y. K. Kuznetsov, and I. L. Nascimento, *Phys. Plasmas* **15**, 112304 (2008).

⁴D. del-Castillo-Negrete, *Phys. Plasmas* **7**, 1702 (2000).

⁵G. Manfredi and R. O. Dendy, *Phys. Rev. Lett.* **76**, 4360 (1996).

⁶J. J. Martinell and D. del-Castillo-Negrete, *Phys. Plasmas* **20**, 022303 (2013).

⁷S. V. Annibaldi, G. Manfredi, and R. O. Dendy, *Phys. Plasmas* **9**, 791 (2002).

⁸G. Manfredi and R. Dendy, *Phys. Plasmas* **4**, 628 (1997).

⁹K. Gustafson, D. del-Castillo-Negrete, and W. Dorland, *Phys. Plasmas* **15**, 102309 (2008).

¹⁰D. del-Castillo-Negrete and J. J. Martinell, *Commun. Nonlinear Sci. Numer. Simul.* **17**, 2031 (2012).

¹¹W. Horton, *Plasma Phys. Controlled Fusion* **27**, 937 (1985).

¹²W. W. Lee, *J. Comput. Phys.* **72**, 243 (1987).

¹³G. A. Oda and I. L. Caldas, *Chaos, Solitons Fractals* **5**, 15 (1995).

¹⁴R. Balescu, *Phys. Rev. E* **58**, 3781 (1998).

¹⁵D. del-Castillo-Negrete and P. J. Morrison, *Bull. Am. Phys. Soc., Series II* **37**, 1543 (1992).

¹⁶L. Nasi and M.-C. Firpo, *Plasma Phys. Controlled Fusion* **51**, 045006 (2009).

¹⁷D. del-Castillo-Negrete and P. J. Morrison, *Phys. Fluids A* **5**, 948 (1993).

¹⁸F. J. Beron-Vera, M. J. Olascoaga, M. G. Brown *et al.*, *Chaos* **20**, 017514 (2010).

¹⁹M. V. Budyansky, M. Y. Uleysky, and S. V. Prants, *Phys. Rev. E* **79**, 056215 (2009).

²⁰D. del-Castillo-Negrete, J. M. Greene, and P. J. Morrison, *Physica D* **91**, 1 (1996).

²¹I. I. Rypina, M. G. Brown *et al.*, *Phys. Rev. Lett.* **98**, 104102 (2007).

²²J. S. E. Portela, I. L. Caldas *et al.*, *Int. J. Bifurcation Chaos Appl. Sci. Eng.* **17**, 1589 (2007).

²³J. D. Szezech, I. L. Caldas *et al.*, *Chaos* **19**, 043108 (2009).

²⁴I. L. Caldas, R. L. Viana *et al.*, *Commun. Nonlinear Sci. Numer. Simul.* **17**, 2021 (2011).

²⁵A. Delshams and R. de-la-Llave, *SIAM J. Math. Anal.* **31**, 1235 (2000).

²⁶E. G. Altmann, G. Cristadoro, and D. Paz, *Phys. Rev. E* **73**, 056201 (2006).

²⁷Y. Zou, D. Paz *et al.*, *Phys. Rev. E* **76**, 016210 (2007).

²⁸C. V. Abud, Ph.D. thesis, University of São Paulo, 2013.

²⁹D. R. Nicholson, *Introduction to Plasma Theory*, (John Wiley and Sons, Inc., New York, 1983).

³⁰W. Horton, H.-B. Park, J.-M. Kwon, D. Strozzi, P. J. Morrison, and D.-I. Choi, *Phys. Plasmas* **5**, 3910 (1998).

³¹B. V. Chirikov, *Phys. Rep.* **52**, 263 (1979).

³²J. B. Taylor, Culham Laboratory Progress Report CLM-PR-12, 1969.

³³J. D. Meiss, *Rev. Mod. Phys.* **64**, 795 (1992).

³⁴J. M. Greene, *J. Math. Phys.* **20**, 1183 (1979).

³⁵S. Shinohara and Y. Aizawa, *Prog. Theor. Phys.* **97**, 379 (1997).

³⁶E. Petrisor, *Int. J. Bifurcation Chaos* **11**, 497 (2001).

³⁷A. Wurm, A. Apte *et al.*, *Chaos* **15**, 023108 (2005).

³⁸N. Slater, *Proc. Cambridge Philos. Soc.* **63**, 1115 (1967).

³⁹J. M. Finn, *Nucl. Fusion* **15**, 845 (1975).

⁴⁰Here, we borrow the definition presented in Ref. 27 of the binary matrix R. Its graphical representation, called recurrence plot, can be used to analyze the recurrence properties of any dynamical system.